

**This item is the archived peer-reviewed author-version of:**

Quantitative analysis of hepatic macro- and microvascular alterations during cirrhogenesis in the rat

**Reference:**

Peeters Geert, Debbaut Charlotte, Friebe Adrian, Cornillie Pieter, De Vos Winnok, Favere Kasper, Vander Elst Ingrid, Vandecasteele Tim, Johann Tim, Van Hoorebeke Luc, ....- Quantitative analysis of hepatic macro- and microvascular alterations during cirrhogenesis in the rat  
Journal of anatomy - ISSN 0021-8782 - 232:3(2018), p. 485-496  
Full text (Publisher's DOI): <https://doi.org/10.1111/JOA.12760>  
To cite this reference: <https://hdl.handle.net/10067/1473460151162165141>

1 **Quantitative image-based analysis of macro- and microvascular**  
2 **morphological alterations during cirrhogenesis in the rat**

3 Geert Peeters<sup>1</sup>, Charlotte Debbaut<sup>1</sup>, Pieter Cornillie<sup>2</sup>, Winnok H. De Vos<sup>3,4</sup>, Kasper Favere<sup>1</sup>,  
4 Ingrid Vander Elst<sup>5</sup>, Tim Vandecasteele<sup>2</sup>, Thomas De Schryver<sup>6</sup>, Diethard Monbaliu<sup>7,8</sup>, Wim  
5 Laleman<sup>5,9</sup> and Patrick Segers<sup>1</sup>

6

7 <sup>1</sup> IBiTech – bioMMeda, Department of Electronics and Information Systems, Ghent University.

8 <sup>2</sup> Department of Morphology, Faculty of Veterinary Medicine, Ghent University.

9 <sup>3</sup> Lab. Cell Biology and Histology, Department of Veterinary Sciences, University of Antwerp.

10 <sup>4</sup> Cell Systems and Imaging, Department of Molecular Biotechnology, University of Ghent.

11 <sup>5</sup> Department of Clinical and Experimental Medicine, KU Leuven

12 <sup>6</sup> Centre for X-Ray Tomography, Department of Physics and Astronomy, Ghent University.

13 <sup>7</sup> Department of Microbiology and Immunology, KU Leuven

14 <sup>8</sup> Department of Abdominal Transplant Surgery, University Hospitals Leuven.

15 <sup>9</sup> Department of Gastroenterology and Hepatology, University Hospitals Leuven.

16

17

18 **Abstract**

19 Cirrhosis represents the end-stage of any persistent chronically active liver disease. It is  
20 characterized by the complete replacement of normal liver tissue by fibrosis, regenerative  
21 nodules, and complete fibrotic vascularized septa. The resulting angio-architectural distortion  
22 contributes to an increasing intrahepatic vascular resistance (IHVR), impeding liver perfusion  
23 and leading to portal hypertension.

24 To date, knowledge on the dynamically evolving pathological changes of the hepatic  
25 vasculature during cirrhogenesis remains limited. More specifically, detailed anatomical data  
26 of the vascular adaptations during disease development is lacking. To address this need, we  
27 studied the 3D architecture of the hepatic vasculature during induction of cirrhogenesis in a rat  
28 model. Cirrhosis was chemically induced with thioacetamide (TAA). At predefined time points,  
29 the hepatic vasculature was fixed and visualized using a combination of vascular corrosion  
30 casting and deep tissue microscopy. 3D reconstruction and data fitting enabled extracting  
31 cirrhotic features at multiple scales, portraying the impact of cirrhosis on the hepatic  
32 vasculature. At the macrolevel, we noticed that regenerative nodules severely compressed pliant  
33 venous vessels from 12-week TAA intoxication onwards. Especially hepatic veins were highly  
34 affected by this compression, with collapsed vessel segments severely reducing perfusion  
35 capabilities. At the microlevel, we discovered zone-specific sinusoidal degeneration with  
36 sinusoids located near the surface being more affected than those in the middle of a liver lobe.  
37 Our data sheds light on and quantifies the evolving angioarchitecture during cirrhogenesis.  
38 These findings may prove helpful for future targeted invasive interventions.

39

40 **Keywords:** cirrhosis, hepatic vasculature, 3D reconstruction, vascular corrosion casting,  
41 immunohistochemistry, confocal laser scanning, micro-CT-scanning, morphological analysis,  
42 rat liver

## 43 **Introduction**

44 Cirrhosis is the common end-point of any given progressive chronic active liver disease and  
45 can evolve to liver insufficiency and clinically significant portal hypertension [1]. Portal  
46 hypertension (PHT) is responsible for the more severe and often lethal complications of  
47 cirrhosis such as bleeding oesophageal varices, ascites, renal dysfunction and hepatic  
48 encephalopathy. Because of the combined impact of these complications, PHT remains the most  
49 important cause of morbidity and mortality in patients with cirrhosis. Not surprisingly, cirrhosis  
50 therefore accounts for approximately 1.03 million deaths per year worldwide [2]. Moreover, 31  
51 million disability adjusted life years (DALYs), equivalent to 1.2% of the global DALY burden,  
52 are attributed to this chronic condition [3].

53 Since the common pathway to cirrhosis entails repetitive destruction and regeneration of liver  
54 tissue, morphological characteristics of cirrhosis comprise diffuse fibrogenesis and the  
55 conversion of the normal liver architecture into structural abnormal regenerative nodules [4].

56 The morphological remodeling exerts a mechanical impact on each of the large hepatic venous  
57 vessels, as these pliant veins, i.e. the portal vein (PV), intrahepatic inferior vena cava inferior  
58 (IVC) and hepatic veins (HVs) are highly amenable for mechanical compression [5-7]. This  
59 architectural distortion contributes to an increased hepatic vascular resistance (IHVR) and is  
60 generally accountable for approximately 70% of the increase in portal pressure in liver cirrhosis  
61 potentially leading to portal hypertension [8, 9].

62 The morphological impact of cirrhosis is also conspicuous at the level of the hepatic  
63 microcirculation [10]. The microvascular phenotype is transformed from highly specialized  
64 porous sinusoids into continuous, more rigid capillaries, a process termed sinusoidal  
65 capillarization with a uniform defenestration of the endothelial cells and development of  
66 subendothelial basal membranes [11, 12]. In addition, cirrhosis causes numerous microscopic  
67 vessel aberrations. Hepatic arterial (HA), portal venous and hepatic venous vessels may tangle

68 with each other. Various distorted spatial arrangements have been reported in blood vessels of  
69 cirrhotic livers, such as sharp bends, anomalous branching patterns, abnormal branching angles  
70 and tortuosity. Severe damage (characterised by bridging fibrosis) results in stenosis and  
71 eventually loss of vessels. In contrast, new vessels may originate to support the blood supply  
72 and venous drainage of the regenerative nodules. The resulting neovasculature is primarily  
73 located in the fibrotic regions which bypasses functional liver tissue and further aggravates liver  
74 insufficiency [13-17]. Furthermore, cirrhosis is considered the principal cause of intrahepatic  
75 portosystemic shunts [18]. However, the majority of portosystemic shunts observed in portal  
76 hypertension are extrahepatic, in an attempt to alleviate the raised portal pressure [19-21]. Non-  
77 tumorous arteriportal shunts have been described in cirrhosis, as are portal-to-portal venous  
78 shunts, although the latter are considered rare [19, 22, 23].

79 Despite the irrefutable importance of the above described research, knowledge on the  
80 pathological alterations of the hepatic (micro)vasculature during the genesis of cirrhosis is  
81 scanty. In this context, animal models are valuable tools to analyze this disease process in the  
82 most appropriate way. More specifically, the thioacetamide (TAA) model [24] is a reproducible  
83 model of homogenous and macronodular cirrhosis, associated with all the typical features of  
84 cirrhosis, including portal hypertension and a hyperdynamic circulatory state.

85 We aimed at measuring the morphological changes of the hepatic vasculature at different time  
86 points during the TAA-induced cirrhogenesis. Detailed anatomical data of rat livers was  
87 obtained using two complementary, recently optimized techniques [26], namely vascular  
88 corrosion casting (VCC) and deep tissue microscopy (DTM) after immunofluorescence  
89 staining. A quantitative description of the spatiotemporal impact of cirrhosis on the hepatic  
90 vasculature might facilitate a better understanding of the underlying mechanisms, contributing  
91 to the increasing IHVR which eventually leads to complications such as portal hypertension  
92 [24].

## 93 **Materials and methods**

### 94 **A. Animals**

95 Cirrhogenesis was induced by oral administration of thioacetamide (TAA; Sigma-Aldrich,  
96 Bornem, Belgium). Prolonged TAA intoxication causes a stepwise process toward  
97 compensated cirrhosis [24]. At the start of the protocol, 0.03% TAA concentration was added  
98 to the drinking water. Thereafter, TAA concentrations were weekly adapted to keep individual  
99 body weights within the limits of 250 - 300g.

100 Male Wistar rats (n = 38) were randomly divided into 4 groups. Each group consisted of 9  
101 animals, except for the fourth group where 2 extra animals were allocated to accommodate  
102 potential mortality. The animals were kept in cages at a constant temperature and humidity in  
103 a 12h controlled light/dark cycle, with food and water provided ad libitum. Group 1 served as  
104 control group, allowing the baseline description of normal hepatic characteristics. Groups 2 to  
105 4 underwent TAA intoxication for 6, 12 and 18 weeks, respectively. After 6 weeks of  
106 administration, histopathological characteristics corresponded to steatohepatitis with  
107 significant fibrosis. At 12 weeks, the advanced fibrotic stage was attained and eventually, after  
108 18 weeks of intoxication, animals showed homogeneous macronodular cirrhosis [24].

109 At the different time points (0, 6, 12 and 18 weeks), the corresponding group (1-4, respectively)  
110 was sacrificed. Five animals of each group (6 in case of group 4) were assigned to the  
111 combination of vascular corrosion casting (VCC) and micro-CT ( $\mu$ CT) imaging to study the  
112 macrocirculation. Four animals (5 in case of group 4) were allocated to deep tissue microscopy  
113 (DTM) after immunofluorescence staining to capture the microcirculation.

### 114 **B. Vascular corrosion casting**

115 The procedure started with anaesthesia by intraperitoneal injection of 130 $\mu$ l/100g pentobarbital  
116 (Nembutal, Ceva Sante Animale, Brussels, Belgium) and careful exposure of the liver and  
117 surrounding vessels. Anticoagulation was performed through intrasplenic administration of

118 heparin (0.3 ml; 5000u/ml) (Heparine Leo, Leo Pharma, Lier, Belgium). The portal vein (PV)  
119 and abdominal aorta (AA) were injected sequentially and manually with 30 ml and 20 ml of a  
120 polyurethane-based casting resin, respectively. The resin mixture consisted of PU4ii (VasQtec,  
121 Zurich, Switzerland), hardener (VasQtec, Zurich, Switzerland), ethyl methyl ketone (EMK;  
122 Merckx, Darmstadt, Germany) and color dyes (yellow and blue for the hepatic arterial (HA)  
123 and PV system, respectively). The radiocontrast agent Lipiodol (Guerbet, Roissy-CdG, France)  
124 was added to the AA resin to allow a clear distinction between the venous and arterial vascular  
125 trees on  $\mu$ CT images. The thoracic aorta and renal arteries were clamped prior to infusion to  
126 direct the resin flow. Immediately after injection, the thoracic caudal vena cava (CVC) and both  
127 inlet vessels were clamped to prevent resin leakage. The specimen was allowed to polymerize  
128 for 72 hours. Afterwards, the liver tissue was macerated in potassium hydroxide (25% KOH)  
129 for approximately 5 days. The resulting cast was then scanned with X-ray imaging at a  
130 resolution of 40  $\mu$ m using an in-house developed high-resolution  $\mu$ CT scanner (HECTOR,  
131 Centre for X-ray Tomography (UGCT), Ghent University, Belgium). A more elaborate  
132 description of the VCC and  $\mu$ CT protocol was described earlier [25].

### 133 **C. Deep tissue microscopy**

134 Animals were anaesthetized by intraperitoneal injection of 130 $\mu$ l/100g pentobarbital  
135 (Nembutal, Ceva Sante Animale, Brussels, Belgium) and subsequently underwent perfusion  
136 fixation with 4% phosphate-buffered paraformaldehyde. The liver was excised and cut into 350  
137  $\mu$ m thick slices by means of a vibratome (Microm HM650V; Thermo Scientific, Massachusetts,  
138 USA). Slices from the top (up to 2 mm from the surface) and mid (4 – 6mm from the surface)  
139 region of the right middle lobe (RML) were selected for further processing. The obtained slices  
140 were permeabilized following a protocol adapted from Renier *et al.* [26]. After  
141 permeabilization, the samples were immunostained using a generic endothelial marker antibody  
142 (RECA-1; Serotec, Kidlington, UK). The limited antibody penetration and imaging depth

143 inherent to traditional immunohistochemistry (IHC) was tackled by applying an adapted version  
144 of the CUBIC (clear, unobstructed brain imaging cocktails and computational analysis) clearing  
145 protocol after IHC [27]. Subsequent confocal laser scanning (Nikon A1R; Nikon, Tokyo, Japan)  
146 provided detailed volumetric datasets of the microcirculation (voxel resolution of  $(0.63 \times 0.63$   
147  $\times 1.4) \mu\text{m}^3$ ) using a 40x Plan Fluor air lens with extra-long working distance (numerical aperture  
148 0.6; working distance 3.6-2.8mm; Nikon Instruments, Paris, France), which were further  
149 processed and analyzed using in-house developed software. For more elaborate details on the  
150 DTM protocol, the reader is referred to [25].

#### 151 **D. Data analysis of the macrocirculation**

152 The  $\mu\text{CT}$  datasets were processed using the commercial software package Mimics (Materialise,  
153 Leuven, Belgium). Vascular trees (HA, PV and HV) were semi-automatically segmented as  
154 their grey value ranges mutually differed in the  $\mu\text{CT}$  images. The arterially added contrast agent  
155 allowed distinguishing the PV from the HA system, and also assigned a different grey value  
156 range to the HV system due to mixing of the injected AA (with contrast agent) and PV resin.  
157 After segmentation, skeletons of the vascular trees were calculated and converted to graphs  
158 using in-house developed software [25]. These graphs were used to quantify the branching  
159 topology and geometrical attributes (branch radius, length and number of vessels). A diameter-  
160 defined top-down ordering method was implemented, partially based on the method used by  
161 Jiang et al. [28], to assign generation numbers to the different branches. As opposed to Jiang,  
162 inlets of each vascular tree (HA, PV and HV) were assigned generation “1” and daughter  
163 branches were allocated generation numbers higher than (or equal) to their parent vessel [25].  
164 After data classification, exponential trend lines were fitted to the morphological features  
165 (radius, length, number of vessels) as a function of their generation number. The fitting  
166 principle was similar to previous studies [29, 30], and allowed quantifying the cirrhogenic  
167 evolution of the parameters studied. Regarding the number of vessels for each generation, trend

168 lines were fitted based on the first 4 generations of the PV and HV (and 3 in case of HA) and  
169 then further extrapolated. In this way, an inaccuracy of the number of vessels due to under-  
170 segmentation was limited.

#### 171 **E. Data analysis of the microcirculation**

172 Prior to microvascular segmentation, DTM datasets were post-processed to reduce lipofuscin-  
173 like autofluorescence, which was abundantly present from 12 weeks of TAA administration  
174 onwards. Practically, autofluorescence was separately recorded for every sample. The resulting  
175 autofluorescence signal was subsequently subtracted from the signal of the vasculature. In  
176 addition, we applied contrast enhancement, denoising and deconvolution to eliminate imaging  
177 noise and reattribute out-of-focus components [31, 32].

178 Segmentation of the microcirculation was executed automatically using in-house developed  
179 software. The segmented datasets allowed for accurate 3D reconstructions of the intertwined  
180 and interconnected blood vessels. Centerlines were calculated for each vessel to extract and  
181 quantify various morphological parameters. The *radius* was measured using a best-fit diameter  
182 approach, which was achieved by measuring the radius in 8 radially evenly distributed  
183 directions. By averaging over the 8 radii, the best-fit radius was able to account for the  
184 ellipsoidal character of blood vessels. *Branch lengths* were calculated as the cumulative  
185 distance between vessel intersections. The *tortuosity* of a branch was defined as the ratio of the  
186 total branch length to the distance between the start and end point of the branch. The 3D *porosity*  
187 of the vascular network was calculated as the total vascular volume divided by the volume of  
188 its envelope. More information on the segmentation and analysis pipeline can be found in [25].  
189 Statistical analyses were performed in R (open source language). Non-parametric Kruskal-  
190 Wallis tests were executed with Holm-Bonferroni adjustment to assess the sinusoidal  
191 remodeling during cirrhogenesis. Differences with a p-value below 0.05 were considered

192 statistically significant. Post hoc pairwise multiple comparison used the Conover-Iman test,  
193 which is robust for small sample sizes.

## 194 **Results**

195 As illustrated by *Fig. 1A-B*, rat livers were excised and casted at different time points during  
196 cirrhogenesis. The macroscopic expression of the liver clearly evolved from normal over an  
197 irregular ‘salt & pepper’-like appearance (6 weeks) to an emerging nodular (12 weeks) and  
198 eventually macronodular liver at 18 weeks. These changing appearances were accurately  
199 captured by the casting procedure, as nodules appeared at the liver’s surface from 12 weeks  
200 onwards.

### 201 **A. Macrocirculation**

#### 202 **Cirrhosis affects mainly the hepatic venous vessels**

203 For each time point, two liver casts were processed down to a 3D reconstruction of all vascular  
204 trees (HA, PV, and HV) (*Fig. 1C-E*). From 12-week intoxication onwards, regenerative nodules  
205 started to mechanically compress their surroundings, which aggravated due to their  
206 continuously growing dimensions. The pliant HV branches were largely affected by this  
207 mechanical compression, and even appeared to collapse as evidenced from the scanned casts  
208 (*Fig. 2B*). In the cirrhotic stage, the PV system was also affected by the nodular compression,  
209 albeit to a lesser extent, and several portosystemic shunt vessels were detected, connecting the  
210 trunk of PV with the CVC (*Fig. 2C*, color-coded in magenta). Furthermore, we observed that  
211 HA branches became more tortuous due to cirrhosis as sudden sharp bends appeared which  
212 were not observed in the control group. However, the HA cross-sections remained unaffected  
213 by the nodular compression, most likely because arterial vessel walls include a thick muscle  
214 layer (*Fig. 2D*).

#### 215 **Regenerative nodules mechanically compress the hepatic venous trees**

216 The vascular trees were classified according to their diameter-defined branching topology. Due  
217 to the restricted  $\mu$ CT resolution, fewer blood vessel generations were measured for the HA  
218 systems, as HA branches normally have smaller diameters than venous branches. For each  
219 generation, the mean radius, length and number of vessels were measured (*Fig. 3*).

220 At the 6-week time point, all vascular trees (HA, PV, HV) appeared unaffected as their  
221 morphological parameters (radii, length, and number vessels) were comparable to control  
222 values. From the 12-week time point, when regenerative nodules began to grow in expansive  
223 manner, radii of the HV gradually decreased. Illustrative is the significant decline of the CVC  
224 radius, dropping from 3.01 mm (healthy) to 1.39 mm (most severe case of cirrhosis) (see  
225 appendix Table 1).

226 The PV system was less affected by cirrhosis. The PV inlet radius marginally dilated from 1.28  
227 mm (rat 1 and 2) to 1.71 mm (rat 7) with increasing intoxication time. However, in rat 8  
228 (presumably a more advanced cirrhotic stage), the PV inlet radius narrowed to 1.01mm (shown  
229 in appendix Table 2). Moreover, a clear widening of the arterial tree was measured during  
230 cirrhogenesis (see appendix Table 3), as the HA inlet radius dilated from  $1.71 \times 10^{-1}$  mm (rat  
231 2) to  $3.01 \times 10^{-1}$  mm (rat 7) (depicted in appendix Table 3).

232 We did not observe any trends in the progression of cirrhogenesis for the number of vessels and  
233 length in function of the generation number. The mean lengths did not even show clear-cut  
234 declining trends in the first generation(s), but started to decrease in higher generations. In  
235 addition, the length of the first generation was underestimated as it was partially cut during  
236 resection of the liver. Therefore, the length of the first generation was not considered when  
237 fitting the trend lines in *Fig. 3B*.

238

## 239 **B. Microcirculation**

### 240 **Cirrhogenesis instigates remodeling of the microcirculation**

241 For each time point, ten to maximally thirteen DTM samples (randomly selected from four  
242 livers with a minimum of two samples/liver) were post-processed, 3D reconstructed and  
243 subjected to pairwise comparison (*Fig. 4A-B*). For the 12-week and 18-week samples, we  
244 differentiated between sinusoids in regenerative nodules and shunt vessels in the fibrotic septa,  
245 both constituting the microcirculation. This was achieved by pre-imaging the slices at a lower  
246 resolution (2.48  $\mu\text{m}$ ; x10 magnification), allowing visual recognition of nodules and  
247 vascularized septa. Samples of their respective microcirculation were subsequently gathered by  
248 scanning both structures individually at a higher resolution (0.63  $\mu\text{m}$ ; x40 magnification).  
249 Histograms of the sinusoidal radii during disease progression are displayed in *Fig. 4C*. The  
250 mean radius decreased from  $4.45 \pm 0.23 \mu\text{m}$  in the control animals to  $3.87 \pm 0.47 \mu\text{m}$  at week  
251 18 ( $p = 0.0047$ ). In addition, the porosity (i.e. the sinusoidal volume per unit of volume) steadily  
252 declined from  $20.43 \pm 1.92\%$  (control) to  $11.12 \pm 3.06\%$  (week 18) ( $p < 10^{-8}$ ) (see *Fig. 4D*).  
253 The sinusoidal tortuosity and length increased slightly but significantly ( $p < 10^{-5}$ ) during  
254 cirrhogenesis going from  $1.12 \pm 0.01$  to  $1.19 \pm 0.05$  and  $18.67 \pm 0.83 \mu\text{m}$  to  $23.95 \pm 4.39 \mu\text{m}$ ,  
255 respectively from week 0 to week 18 (see *Fig. 5*).

#### 256 **Cirrhosis affects the sinusoidal network zone-specifically**

257 Samples sectioned near the top ( $n \geq 5$ ) were compared to samples located in the middle of the  
258 RML ( $n \geq 5$ ). We found that sinusoids situated in the core of the lobe typically had larger radii  
259 and appeared less affected by the cirrhotic process compared to those near the surface (*Fig.*  
260 *6*). Pairwise comparison of the 18-week samples demonstrated significantly different radii in  
261 these 2 zones ( $p = 0.048$ ). Variations between the porosity of mid- and top-located samples  
262 existed, but did not vary significantly. Similar observations were made for the branch length  
263 and tortuosity.

#### 264 **Cirrhosis is characterized by the formation of highly vascularized fibrous septa**

265 We analyzed several samples consisting primarily of vascular septa in case of cirrhosis (n=3)  
266 and compared their radial histogram with those of cirrhotic sinusoids (*Fig. 4D*). The skewed  
267 distribution of the vascular septa indicated the presence of very large blood vessels (radius >  
268 10  $\mu\text{m}$ ) acting as intrahepatic shunts. The septa also comprised a substantial amount of smaller  
269 intertwined blood vessels, which probably originated to support blood supply. Both vessel types  
270 are embedded in fibrotic tissue and thus separated from the hepatocytes. They act as bypasses  
271 guiding the blood flow directly from the portal tract into the central vein.

## 272 **Discussion**

273 The present study is, to the best of our knowledge, the first to analyze the main remodeling  
274 events of the hepatic vascular architecture during TAA cirrhogenesis in rats. Solely using static  
275 techniques (VCC and DTM), we were able to study and quantify the dynamic transition of this  
276 pathological process. At 4 discrete time points during the progression toward cirrhosis, VCC  
277 and DTM were used to capture, 3D reconstruct and morphologically analyze the intricate  
278 hepatic vasculature across multiple length scales. Our data demonstrated various anatomical  
279 abnormalities attributable to cirrhosis, which are likely to underlie the increase of total IHVR  
280 as previously characterized hemodynamically in this model and at the same given time points  
281 [24].

282 With VCC, we examined the circulatory changes at the macrolevel. From 12-week TAA  
283 intoxication onwards, regenerative nodules started to grow in an expansive manner. It is  
284 commonly assumed that this tissue growth exerts a compressive force on the surrounding blood  
285 vessels (*Fig. 2*). This compression narrowed the pliant venous systems (PV and HV), but we  
286 found that especially the HV was highly impacted by this compression, with collapsed vessel  
287 segments severely impeding hepatic outflow (*Fig. 3*). The mean diameters of the HV across the  
288 first generations nearly halved. As resistance of a vessel scales inversely with its radius to the  
289 fourth power following Poiseuille's law, it is not surprising that an increase of the total IHVR  
290 was documented in TAA-induced cirrhotic livers [24].

291 Furthermore, the HA dilated with increasing intoxication time. The diameter of the PV most  
292 likely increased up until the moment the mechanical impact of the regenerative nodules  
293 outweighed the internal portal pressure and forced the PV to narrow, as observed in rat 8 (more  
294 advanced stage of cirrhosis). Narrowing of the HV and PV vasculature contributed to the ever-  
295 increasing IHVR and hepatic venous pressure gradient (HVPG) over the liver in cirrhosis [24].

296 At the microscopic level, sinusoidal remodeling was abundantly present. Capillarization and  
297 the impaired intrahepatic balance between vasodilators and -constrictor presumably caused the  
298 diameters and number of sinusoids to decrease [10]. We observed that, from 12 weeks onwards,  
299 the microvascular porosity and sinusoidal radii differed significantly from control data at week  
300 0 (*Fig. 4C* and *Fig. 5A-B*). Even though macrocirculatory changes were still limited, portal  
301 hypertension was already measured at 12 weeks as document earlier in the animal model [24].  
302 This suggests that the increase of the IHVR is initiated at the microlevel and is further  
303 aggravated by alterations at the macroscale later on. At 18 weeks, portal hypertension became  
304 associated with a hyperdynamic circulatory state (another pathophysiological hallmark of  
305 cirrhosis), which may have further contributed to the increasing portal pressure [24]. At 18  
306 weeks of TAA, the presence of complete fibrous vascularized septa was previously reported,  
307 which encapsulate growing regenerative nodules [24]. In the present work, we observed that  
308 these portal-portal and portal-central septa comprised a considerable amount of small vessels  
309 as well as larger intrahepatic shunt vessels (*Fig. 4C*). Additionally, intrahepatic portosystemic  
310 shunts were detected between the trunk of the PV and CVC (*Fig. 2C*). These shunt vessels most  
311 likely developed in an attempt to alleviate the elevated portal pressures, but at the cost of  
312 shunting large amounts of blood directly into the systemic circulation without contact with the  
313 hepatocytes, incapacitating as such synthetic and detoxification liver functions.

314 Although the workflow of this study is straightforward, some aspects are very labor intensive  
315 and time consuming. This is particularly the case for the segmentation of the  $\mu$ CT datasets of  
316 the vascular corrosion casts, which is why only two liver casts were fully segmented for each  
317 cirrhogenic stage. Therefore, it is necessary to consider the reported numerical data as  
318 indicative.

319 Moreover, liver casts should ideally be  $\mu$ CT-scanned at a sufficiently high resolution to allow  
320 reconstructing the HA accurately up to the same generation as the PV. Since diameters of HA

321 branches are typically smaller than PV branches, this was technically impossible with the  
322 current computational capabilities. As a consequence, the number of HA vessels for each  
323 generation was underestimated as smaller ramifying branches remained undetected. Since the  
324 HA runs in parallel with the PV, we can only assume that the number of vessels should be at  
325 least equal to or even higher (due to PV being flanked by more than one parallel HA vessels)  
326 than the PV [30].

327 The hypothesis that the casting resin caused significant tissue shrinkage was discredited. We  
328 presumed that the known shrinkage of the cast resin was compensated by the pressure exerted  
329 during the injection of the polymer [30, 33, 34].

330

### 331 **Conclusion**

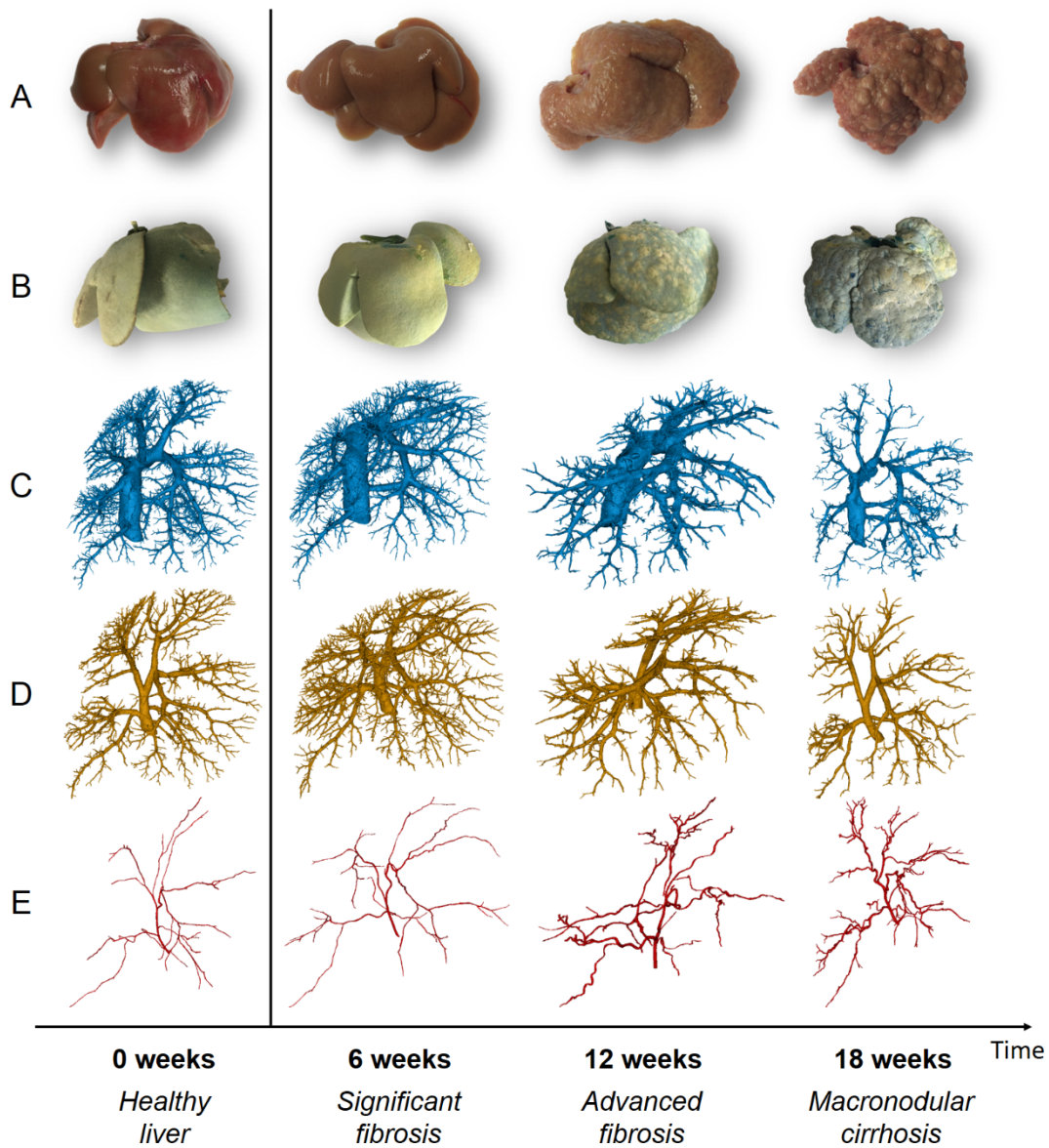
332 Cirrhotic changes of the hepatic vasculature were analyzed and quantified in the TAA cirrhotic  
333 rat model. At predefined time points, two techniques (VCC and DTM) were used to accurately  
334 capture and 3D reconstruct the hepatic vasculature across different scales, ranging from the  
335 largest blood vessels down to the sinusoids. Their complementarity allowed to provide a  
336 comprehensive overview of the impact of cirrhosis on the vasculature, revealing static  
337 mechanisms behind the increased IHVR which were hemodynamically characterized earlier at  
338 similar time points and in the same model [24]. The combined impact of this work, both  
339 hemodynamically as angio-architecturally, might be of interest for targeted liver interventions  
340 both pharmaceutically, surgically and angiographically.

341

342

343

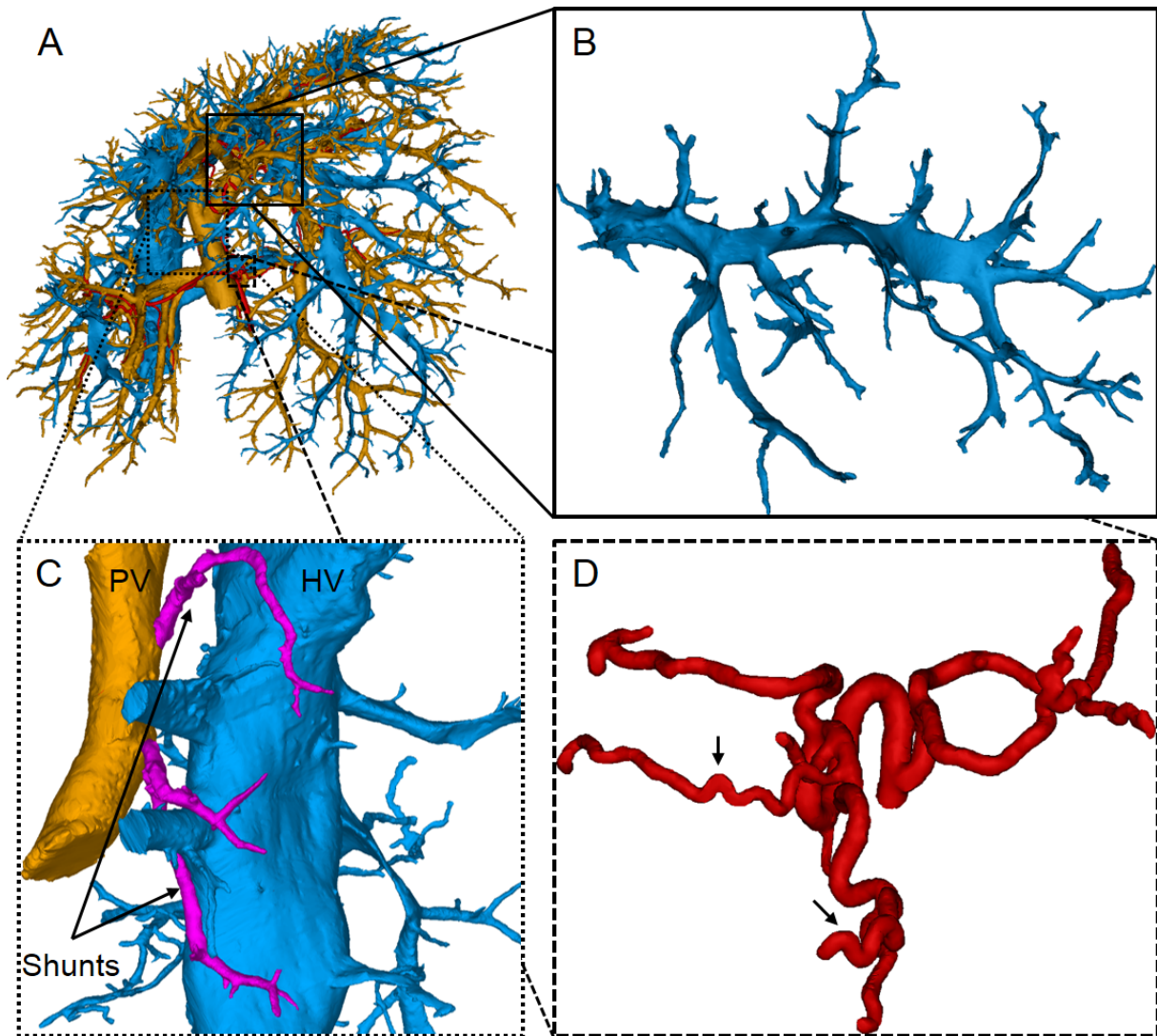
344



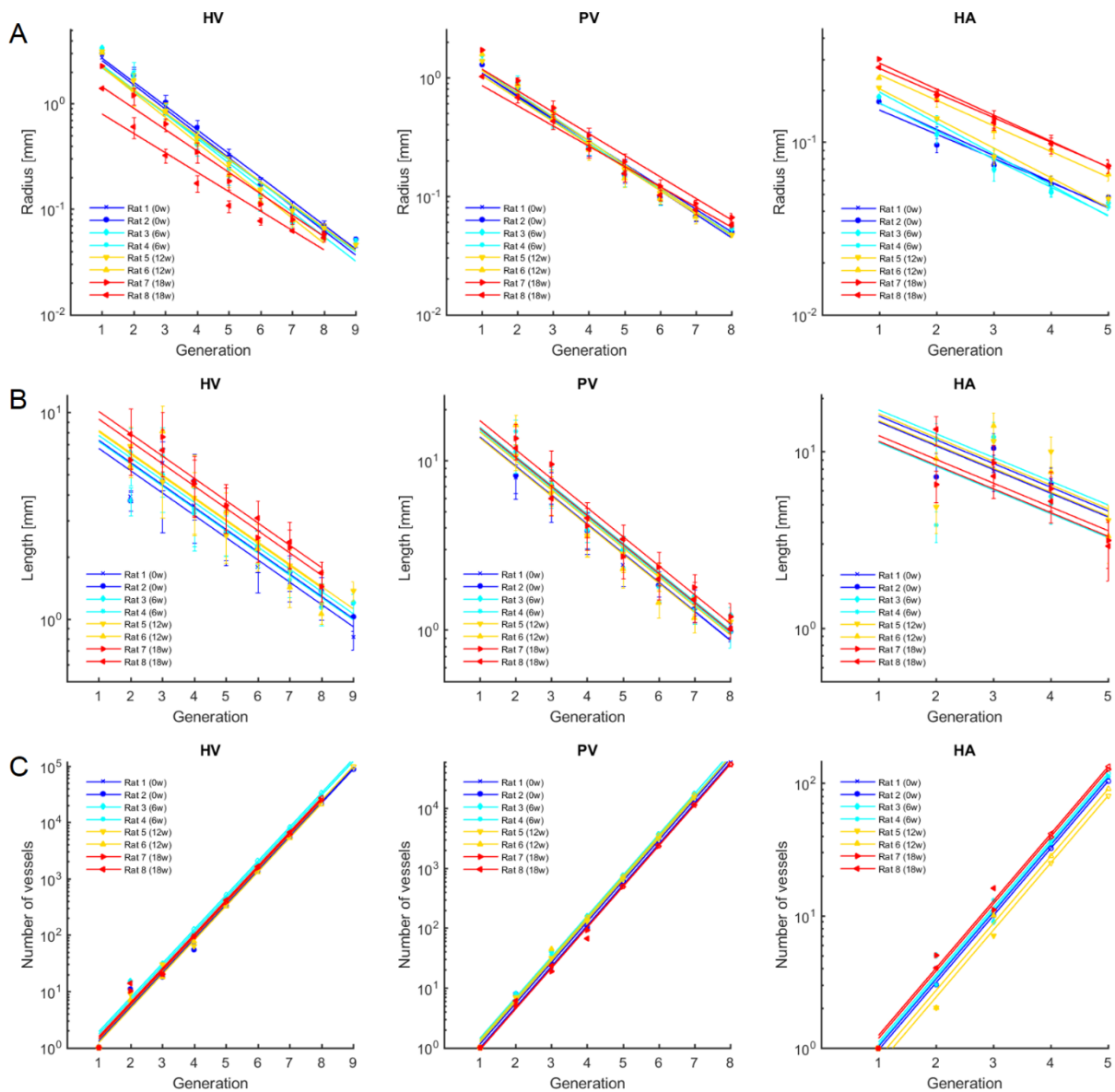
346

347 **Fig. 1. A.** Rat livers were excised at different time points during cirrhogenesis. The right median  
 348 lobe (RML) was sectioned prior to immunostaining. The macroscopic expression of the liver  
 349 transformed from normal over an irregular ‘salt & pepper’-like appearance at 6 weeks to an  
 350 emerging nodular liver at 12 weeks and ultimately macronodular liver at 18 weeks. **B.** Vascular  
 351 replicas obtained using vascular corrosion casting. Blue pigmented resin was injected via the  
 352 PV and yellow dye was added to the arterial resin. **C-E.** 3D reconstructions of the macroscopic

353 hepatic veins (HV), portal veins (PV) and hepatic arteries (HA), respectively, obtained using  
354 vascular corrosion casts.



355  
356 **Fig. 2 A.** Accurate 3D reconstruction of the macrocirculation of a cirrhotic liver (18 weeks). **B.**  
357 The amendable hepatic veins in the middle median lobe (MML) are significantly compressed  
358 by regenerative nodules and some branches even appeared to collapse. **C.** Porto-systemic shunts  
359 were detected, shunting directly from the root of the PV into the HV (CVC). Two branching  
360 trees from the HV were cut to provide a better view of the shunts. **D.** Due to cirrhosis, arterial  
361 branches became more tortuous, resulting in sudden sharp bends (arrows).



362

363 **Fig. 3** The macrovascular trees – hepatic vein (HV), portal vein (PV), and hepatic artery (HA)

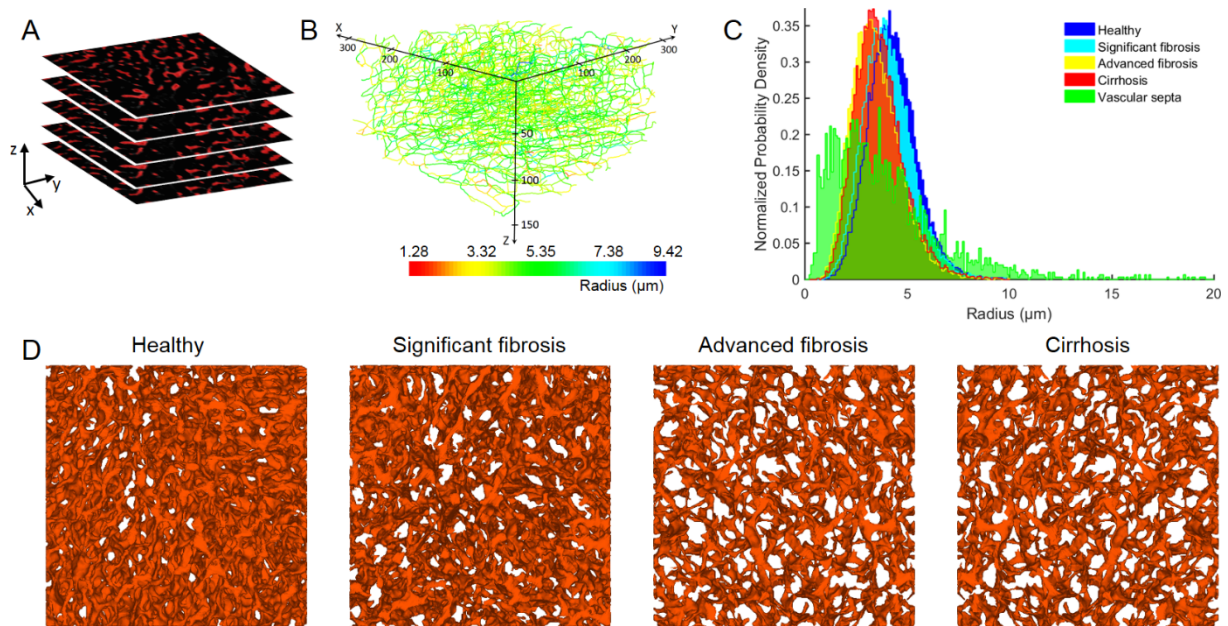
364 – were classified according to their diameter-defined branching topology. For each liver

365 intoxicated with TAA during different weeks (0w, 6w, 12w, 18w), the mean radius (A), length

366 (B), and number of vessels (C) were measured as function of the generation number and

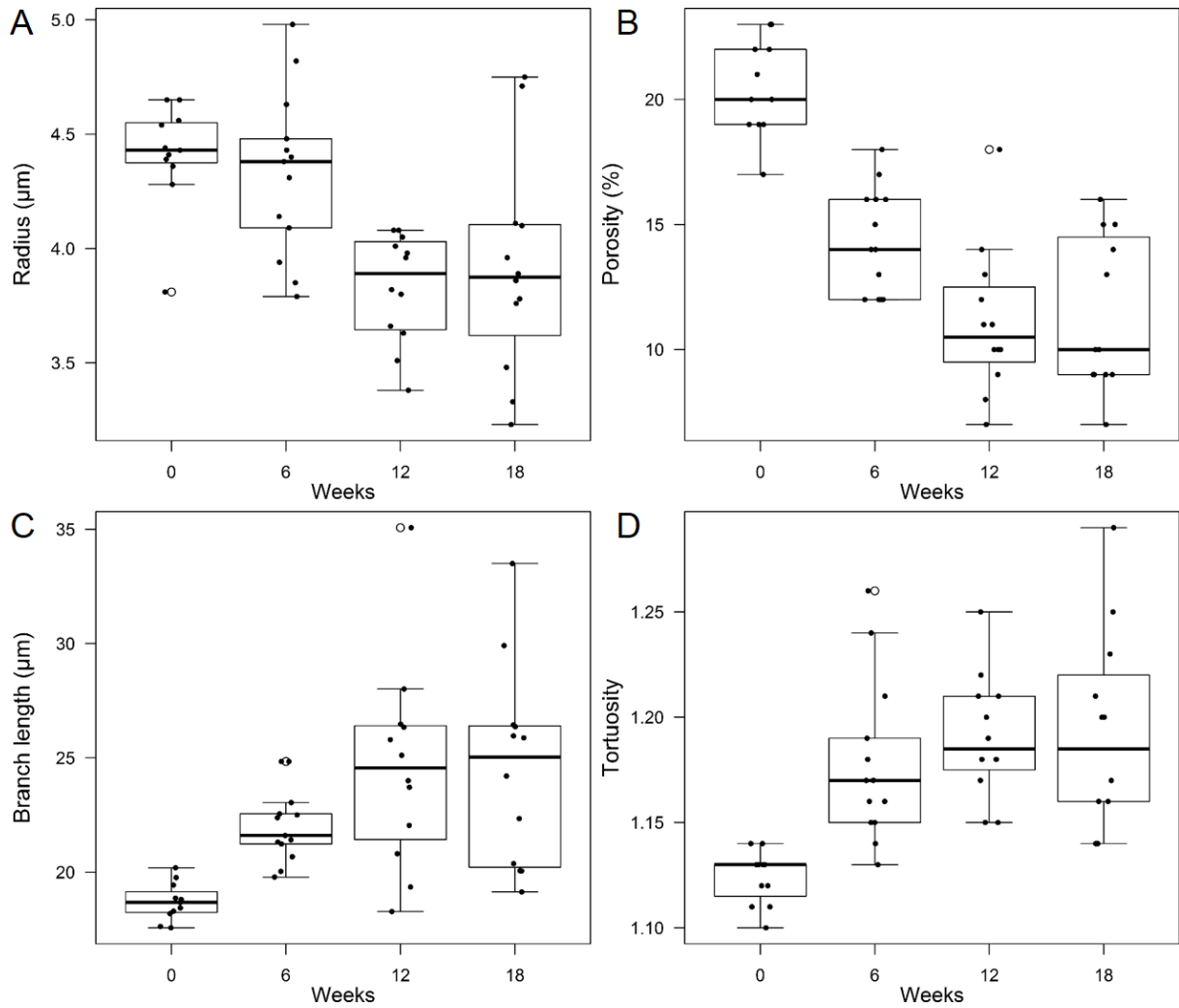
367 exponential trend lines were fitted. Due to mechanical compression of the nodules, cirrhosis

368 appeared to have a high impact on the radius of the HV.



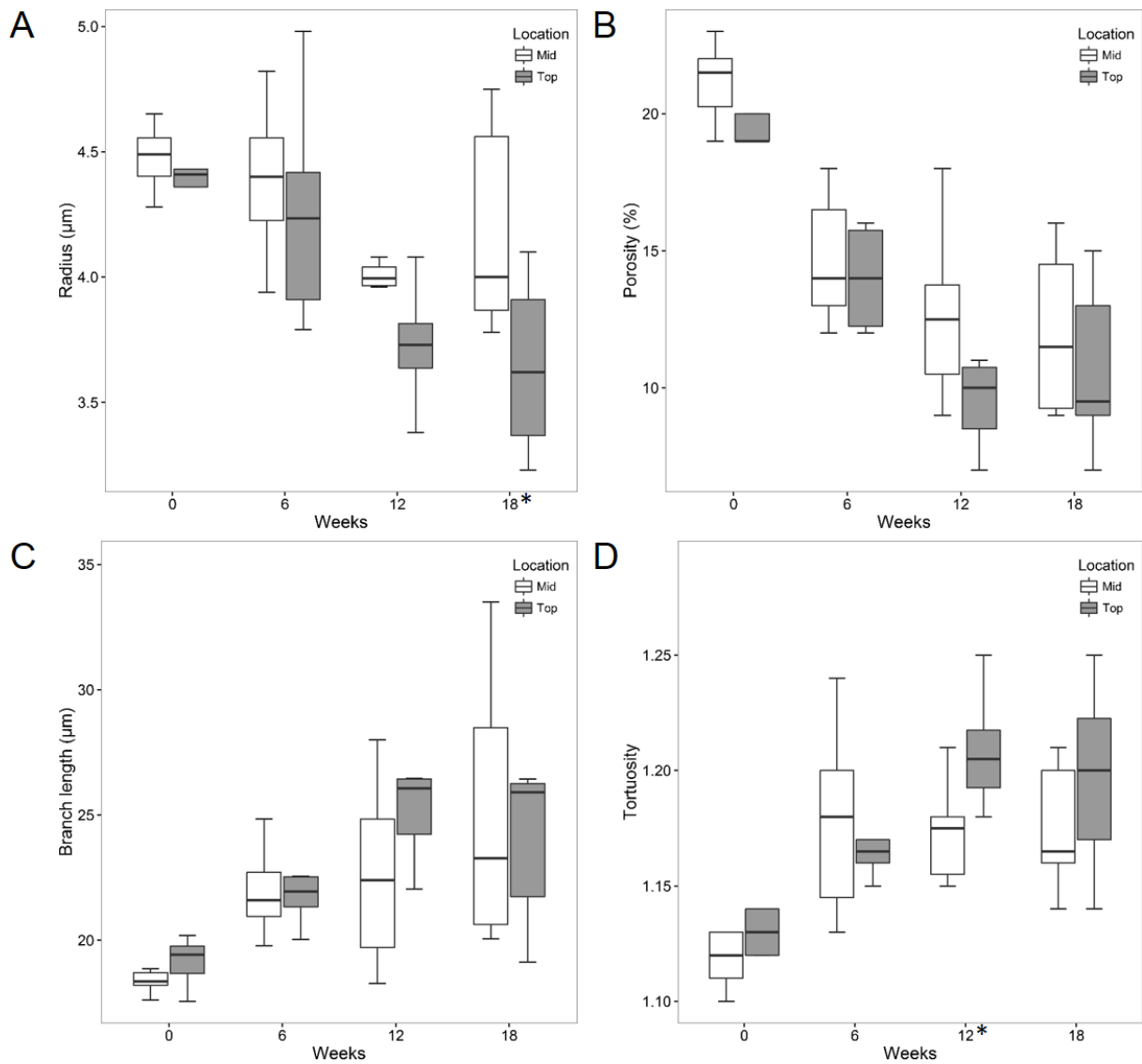
369

370 **Fig. 4. A.** Example of a stack of 2D images acquired through deep tissue microscopy (DTM).  
 371 **B.** The dataset was automatically processed to segment the sinusoidal network and convert it to  
 372 a graph. Here, the network graph is colored according to the mean radius of the branches. The  
 373 graph allowed extracting other morphological parameters, including the length, tortuosity and  
 374 porosity. **C.** Histograms of the sinusoidal radii during the different cirrhotic stages. The  
 375 values visibly shift to the left, when progressing from a normal to a cirrhotic liver. At 12 weeks  
 376 and 18 weeks, we differentiated between the sinusoids in regenerative nodules and the  
 377 microvascular vessels in the vascular septa. These vascular septa consisted of a substantial  
 378 number of smaller vessels, but also a considerable number of large shunt vessels (diameter  $>$   
 379  $10 \mu\text{m}$ ). **D.** 3D reconstructions of the intricate sinusoidal network obtained with DTM ( $140 \mu\text{m}$   
 380 thick samples). The volume of blood vessels per volume unit (=porosity) decreased with  
 381 increasing intoxication time from 19% (normal) over 16% (significant fibrosis) and 9%  
 382 (advanced fibrosis) to 7% (cirrhosis).



383

384 **Fig. 5** Boxplots for the radius (A), porosity (B), branch length (C), and tortuosity (D) of the  
 385 microcirculation in function of TAA intoxication time. The radius and porosity differed  
 386 significantly between normal and cirrhotic livers ( $p < 0.05$ ). Both parameters decreased  
 387 gradually during cirrhotic progression, contributing to the increased intrahepatic vascular  
 388 resistance.



389

390

391 **Fig. 6** Boxplots for the radius (**A**), porosity (**B**), branch length (**C**), and tortuosity (**D**) of the  
 392 microcirculation as a function of TAA intoxication time and location within the lobe. Slices  
 393 ( $350\ \mu\text{m}$ ) were taken near the top (up to 2 mm from the surface) and mid (4 – 6 mm from the  
 394 surface) region of the right middle lobe (RML). Sinusoids situated in the core of the lobe  
 395 appeared to be less affected by the cirrhotogenic process, as their mean radii and porosity were  
 396 typically larger than those near the surface. When comparing the 18-week intoxicated samples  
 397 pairwise, the radii even differed significantly between the top and mid region ( $p = 0.048$ ).

398

399 **References**

- 400 1. Pinzani, M., M. Rosselli, and M. Zuckermann, *Liver cirrhosis*. Best Pract Res Clin Gastroenterol, 2011. **25**(2): p. 281-90.
- 401
- 402 2. Tsochatzis, E.A., J. Bosch, and A.K. Burroughs, *Liver cirrhosis*. Lancet, 2014. **383**(9930): p. 1749-403 1761.
- 404 3. Mokdad, A.A., et al., *Liver cirrhosis mortality in 187 countries between 1980 and 2010: a 405 systematic analysis*. BMC Med, 2014. **12**: p. 145.
- 406 4. Anthony, P.P., et al., *The morphology of cirrhosis. Recommendations on definition, 407 nomenclature, and classification by a working group sponsored by the World Health 408 Organization*. J Clin Pathol, 1978. **31**(5): p. 395-414.
- 409 5. Levy AD, M.K., Yeh, BM, *Gastrointestinal Imaging*. 2015, USA: Oxford University Press.
- 410 6. Ismail, M.H. and M. Pinzani, *Reversal of liver fibrosis*. Saudi J Gastroenterol, 2009. **15**(1): p. 72-411 9.
- 412 7. Yamamoto, T., T. Kobayashi, and M.J. Phillips, *Perinodular arteriolar plexus in liver cirrhosis. 413 Scanning electron microscopy of microvascular casts*. Liver, 1984. **4**(1): p. 50-4.
- 414 8. Hu, L.S., J. George, and J.H. Wang, *Current concepts on the role of nitric oxide in portal 415 hypertension*. World J Gastroenterol, 2013. **19**(11): p. 1707-17.
- 416 9. Laleman, W., et al., *Portal hypertension: from pathophysiology to clinical practice*. Liver Int, 417 2005. **25**(6): p. 1079-90.
- 418 10. Thabut, D. and V. Shah, *Intrahepatic angiogenesis and sinusoidal remodeling in chronic liver 419 disease: New targets for the treatment of portal hypertension?* Journal of Hepatology, 2010. 420 **53**(5): p. 976-980.
- 421 11. Braet, F. and E. Wisse, *Structural and functional aspects of liver sinusoidal endothelial cell 422 fenestrae: a review*. Comp Hepatol, 2002. **1**(1): p. 1.
- 423 12. Huet, P.M., et al., *Assessment of liver microcirculation in human cirrhosis*. J Clin Invest, 1982. 424 **70**(6): p. 1234-44.
- 425 13. Debbaut, C., *Multi-Level modelling of hepatic perfusion in support of liver transplantation 426 strategies*. 2013, Ghent University: Ghent.
- 427 14. Kline, T.L., et al., *Anatomy of hepatic arteriolo-portal venular shunts evaluated by 3D micro-CT 428 imaging*. J Anat, 2014. **224**(6): p. 724-31.
- 429 15. Hano, H. and S. Takasaki, *Three-dimensional observations on the alterations of lobular 430 architecture in chronic hepatitis with special reference to its angioarchitecture for a better 431 understanding of the formal pathogenesis of liver cirrhosis*. Virchows Arch, 2003. **443**(5): p. 432 655-63.
- 433 16. Van Steenkiste, C., *The role of the placental growth factor (PlGF) in the pathophysiology of 434 portal hypertension and cirrhosis*. 2010, Ghent University: Ghent.
- 435 17. Vanheule, E., et al., *An intravital microscopic study of the hepatic microcirculation in cirrhotic 436 mice models: relationship between fibrosis and angiogenesis*. Int J Exp Pathol, 2008. **89**(6): p. 437 419-32.
- 438 18. Lutz, J., et al., *Intrahepatic portal-to-portal venous shunts in cirrhosis: a potential mimic of 439 hepatocellular carcinoma*. J Comput Assist Tomogr, 2004. **28**(4): p. 520-2.
- 440 19. Bodner, G., et al., *Nontumorous vascular malformations in the liver: color Doppler 441 ultrasonographic findings*. J Ultrasound Med, 2002. **21**(2): p. 187-97.
- 442 20. Alexander, B., H. Cottam, and R. Naftalin, *Hepatic arterial perfusion regulates portal venous 443 flow between hepatic sinusoids and intrahepatic shunts in the normal rat liver in vitro*. Pflugers 444 Arch, 2001. **443**(2): p. 257-64.
- 445 21. Mori, H., et al., *Intrahepatic portosystemic venous shunt: occurrence in patients with and 446 without liver cirrhosis*. AJR Am J Roentgenol, 1987. **149**(4): p. 711-4.
- 447 22. Kassissia, I., A. Brault, and P.M. Huet, *Hepatic artery and portal vein vascularization of normal 448 and cirrhotic rat liver*. Hepatology, 1994. **19**(5): p. 1189-97.

- 449 23. Bhargava, P., et al., *Pictorial review. Hepatic vascular shunts: embryology and imaging*  
450 *appearances*. Br J Radiol, 2011. **84**(1008): p. 1142-52.
- 451 24. Laleman, W., et al., *A stable model of cirrhotic portal hypertension in the rat: thioacetamide*  
452 *revisited*. Eur J Clin Invest, 2006. **36**(4): p. 242-9.
- 453 25. Peeters, G., et al., *A multilevel framework to reconstruct anatomical 3D models of the hepatic*  
454 *vasculature in rat livers*. J Anat, 2017. **230**(3): p. 471-483.
- 455 26. Renier, N., et al., *iDISCO: a simple, rapid method to immunolabel large tissue samples for*  
456 *volume imaging*. Cell, 2014. **159**(4): p. 896-910.
- 457 27. Susaki, E.A., et al., *Whole-brain imaging with single-cell resolution using chemical cocktails and*  
458 *computational analysis*. Cell, 2014. **157**(3): p. 726-39.
- 459 28. Jiang, Z.L., G.S. Kassab, and Y.C. Fung, *Diameter-defined Strahler system and connectivity*  
460 *matrix of the pulmonary arterial tree*. J Appl Physiol (1985), 1994. **76**(2): p. 882-92.
- 461 29. Debbaut, C., et al., *Modeling the impact of partial hepatectomy on the hepatic hemodynamics*  
462 *using a rat model*. IEEE Trans Biomed Eng, 2012. **59**(12): p. 3293-303.
- 463 30. Debbaut, C., et al., *Analyzing the human liver vascular architecture by combining vascular*  
464 *corrosion casting and micro-CT scanning: a feasibility study*. J Anat, 2014. **224**(4): p. 509-17.
- 465 31. Schindelin, J., et al., *Fiji: an open-source platform for biological-image analysis*. Nat Methods,  
466 2012. **9**(7): p. 676-82.
- 467 32. Luisier, F., T. Blu, and M. Unser, *Image denoising in mixed Poisson-Gaussian noise*. IEEE Trans  
468 Image Process, 2011. **20**(3): p. 696-708.
- 469 33. Kratky, R.G. and M.R. Roach, *Shrinkage of Batson's and its relevance to vascular casting*.  
470 Atherosclerosis, 1984. **51**(2-3): p. 339-41.
- 471 34. Krucker, T., A. Lang, and E.P. Meyer, *New polyurethane-based material for vascular corrosion*  
472 *casting with improved physical and imaging characteristics*. Microsc Res Tech, 2006. **69**(2): p.  
473 138-47.

474

475 **Appendix**

476 **Table 1:** Macroscopic hepatic veins were classified according to their diameter-defined  
 477 branching topology at different time points during cirrhogenesis. The mean radius, mean length  
 478 and number of vessels were measured based on the assignment of generation numbers.

HV	Generation	Mean radius (mm)		Mean length (mm)		#Vessels	
		Rat 1	Rat 2	Rat 1	Rat 2	Rat 1	Rat 2
Healthy liver <i>0 weeks</i>	1	2.73	3.01	27.87	21.43	1	1
	2	1.75 ± 3.36 x 10 <sup>-1</sup>	1.87 ± 3.62 x 10 <sup>-1</sup>	3.92 ± 0.26	3.73 ± 0.39	10	11
	3	9.31 x 10 <sup>-1</sup> ± 1.39 x 10 <sup>-1</sup>	1.04 ± 1.79 x 10 <sup>-1</sup>	5.69 ± 1.52	4.65 ± 2.03	19	18
	4	5.35 x 10 <sup>-1</sup> ± 8.80 x 10 <sup>-2</sup>	5.95 x 10 <sup>-1</sup> ± 1.02 x 10 <sup>-1</sup>	3.53 ± 1.20	4.66 ± 1.64	66	55
	5	2.91 x 10 <sup>-1</sup> ± 4.81 x 10 <sup>-2</sup>	3.13 x 10 <sup>-1</sup> ± 6.01 x 10 <sup>-2</sup>	2.62 ± 0.70	2.59 ± 0.77	224	178
	6	1.64 x 10 <sup>-1</sup> ± 2.97 x 10 <sup>-2</sup>	1.71 x 10 <sup>-1</sup> ± 2.96 x 10 <sup>-2</sup>	1.78 ± 0.43	2.18 ± 0.50	486	451
	7	8.93 x 10 <sup>-2</sup> ± 1.55 x 10 <sup>-2</sup>	1.04 x 10 <sup>-1</sup> ± 1.49 x 10 <sup>-2</sup>	1.50 ± 0.29	1.69 ± 0.33	709	795
	8	5.76 x 10 <sup>-2</sup> ± 5.81 x 10 <sup>-3</sup>	7.00 x 10 <sup>-2</sup> ± 7.77 x 10 <sup>-3</sup>	1.16 ± 0.18	1.37 ± 0.23	356	672
	9	4.47 x 10 <sup>-2</sup> ± 2.09 x 10 <sup>-3</sup>	5.17 x 10 <sup>-2</sup> ± 3.44 x 10 <sup>-3</sup>	0.82 ± 0.11	1.02 ± 0.15	56	138
Significant fibrosis <i>6 weeks</i>	1	3.41	3.07	36.58	23.73	1	1
	2	1.92 ± 5.67 x 10 <sup>-1</sup>	1.78 ± 1.98 x 10 <sup>-1</sup>	6.41 ± 1.98	3.74 ± 0.58	15	15
	3	8.22 x 10 <sup>-1</sup> ± 1.36 x 10 <sup>-1</sup>	8.75 x 10 <sup>-1</sup> ± 1.50 x 10 <sup>-1</sup>	4.99 ± 1.72	6.16 ± 2.28	31	25
	4	4.11 x 10 <sup>-1</sup> ± 8.85 x 10 <sup>-2</sup>	4.66 x 10 <sup>-1</sup> ± 9.02 x 10 <sup>-2</sup>	3.25 ± 1.02	3.41 ± 1.27	134	105
	5	2.08 x 10 <sup>-1</sup> ± 3.90 x 10 <sup>-2</sup>	2.37 x 10 <sup>-1</sup> ± 4.75 x 10 <sup>-2</sup>	2.58 ± 0.58	2.65 ± 0.62	377	280
	6	1.17 x 10 <sup>-1</sup> ± 2.00 x 10 <sup>-2</sup>	1.35 x 10 <sup>-1</sup> ± 2.15 x 10 <sup>-2</sup>	2.25 ± 0.41	2.21 ± 0.44	741	561
	7	7.52 x 10 <sup>-2</sup> ± 9.10 x 10 <sup>-3</sup>	9.10 x 10 <sup>-2</sup> ± 9.20 x 10 <sup>-3</sup>	1.71 ± 0.26	1.55 ± 0.27	679	517
	8	5.40 x 10 <sup>-2</sup> ± 2.68 x 10 <sup>-3</sup>	6.63 x 10 <sup>-2</sup> ± 6.95 x 10 <sup>-3</sup>	1.34 ± 0.14	1.14 ± 0.21	135	208
	9	4.64 x 10 <sup>-2</sup> ± 1.91 x 10 <sup>-3</sup>	5.12 x 10 <sup>-2</sup> ± 1.91 x 10 <sup>-3</sup>	1.20 ± 0.13	1.20 ± 0.13	28	28
Advanced Fibrosis <i>12 weeks</i>	1	3.12	3.04	35.48	32.82	1	1
	2	1.65 ± 2.93 x 10 <sup>-1</sup>	1.35 ± 4.00 x 10 <sup>-1</sup>	6.88 ± 1.62	5.46 ± 0.61	9	7
	3	8.56 x 10 <sup>-1</sup> ± 1.60 x 10 <sup>-1</sup>	8.29 x 10 <sup>-1</sup> ± 1.83 x 10 <sup>-1</sup>	4.62 ± 1.53	8.08 ± 2.63	30	18
	4	4.72 x 10 <sup>-1</sup>	4.31 x 10 <sup>-1</sup>	3.84 ± 1.29	4.39 ± 1.82	63	78

	5	$\pm 7.18 \times 10^{-2}$ $2.68 \times 10^{-1}$	$\pm 9.24 \times 10^{-2}$ $2.10 \times 10^{-1}$	$2.53 \pm 0.67$	$3.30 \pm 0.78$	211	221
	6	$\pm 4.82 \times 10^{-2}$ $1.53 \times 10^{-1}$	$\pm 4.95 \times 10^{-2}$ $1.16 \times 10^{-1}$	$2.36 \pm 0.50$	$2.18 \pm 0.48$	417	324
	7	$\pm 2.44 \times 10^{-2}$ $9.63 \times 10^{-2}$	$\pm 1.66 \times 10^{-2}$ $7.78 \times 10^{-2}$	$1.80 \pm 0.35$	$1.42 \pm 0.28$	521	197
	8	$\pm 1.28 \times 10^{-2}$ $6.64 \times 10^{-2}$	$\pm 9.06 \times 10^{-3}$ $5.38 \times 10^{-2}$	$1.44 \pm 0.24$	$1.06 \pm 0.12$	227	7
	9	$\pm 7.25 \times 10^{-3}$ $4.57 \times 10^{-2}$	$\pm 3.32 \times 10^{-3}$ $\pm 1.93 \times 10^{-3}$	$1.37 \pm 0.15$		6	
		<b>Rat 7</b>	<b>Rat 8</b>	<b>Rat 7</b>	<b>Rat 8</b>	<b>Rat 7</b>	<b>Rat 8</b>
	1	<i>2.77</i>	<i>1.39</i>	<i>23.39</i>	<i>19.26</i>	<i>1</i>	<i>1</i>
	2	1.19	$6.09 \times 10^{-1}$	$5.87 \pm 0.92$	$7.84 \pm 2.53$	10	14
	3	$\pm 2.13 \times 10^{-1}$ $6.38 \times 10^{-1}$	$\pm 1.37 \times 10^{-1}$ $3.26 \times 10^{-1}$	$7.59 \pm 2.43$	$6.56 \pm 1.67$	20	20
	4	$\pm 8.74 \times 10^{-2}$ $3.51 \times 10^{-1}$	$\pm 4.94 \times 10^{-2}$ $1.77 \times 10^{-1}$	$4.51 \pm 1.40$	$4.66 \pm 1.49$	60	93
	5	$\pm 7.48 \times 10^{-2}$ $1.85 \times 10^{-1}$	$\pm 3.11 \times 10^{-2}$ $1.08 \times 10^{-1}$	$3.53 \pm 0.94$	$3.51 \pm 0.81$	148	138
	6	$\pm 3.27 \times 10^{-2}$ $1.12 \times 10^{-1}$	$\pm 1.38 \times 10^{-2}$ $7.69 \times 10^{-2}$	$2.47 \pm 0.58$	$3.08 \pm 0.63$	213	108
	7	$\pm 1.43 \times 10^{-2}$ $7.96 \times 10^{-2}$	$\pm 5.75 \times 10^{-3}$ $6.27 \times 10^{-2}$	$2.22 \pm 0.48$	$2.36 \pm 0.59$	179	21
	8	$\pm 7.48 \times 10^{-3}$ $5.79 \times 10^{-2}$	$\pm 1.53 \times 10^{-3}$ $5.37 \times 10^{-2}$	$1.44 \pm 0.22$	$1.67 \pm 0.21$	80	24
		$\pm 4.86 \times 10^{-3}$	$\pm 4.39 \times 10^{-3}$				
<b>Cirrhosis</b> <i>18 weeks</i>							

479

480

481 **Table 2:** Macroscopic portal veins were classified according to their diameter-defined  
 482 branching topology at different time points during cirrhogenesis. The mean radius, mean length  
 483 and number of vessels were measured based on the assignment of generation numbers.

PV	Generation	Mean radius (mm)		Mean length (mm)		#Vessels	
		Rat 1	Rat 2	Rat 1	Rat 2	Rat 1	Rat 2
Healthy liver <i>0 weeks</i>	1	1.28	1.28	13.41	15.96	1	1
	2	$8.08 \times 10^{-1}$ $\pm 1.13 \times 10^{-1}$	$8.05 \times 10^{-1}$ $\pm 1.17 \times 10^{-1}$	$7.90 \pm 1.52$	$8.14 \pm 2.19$	6	8
	3	$5.08 \times 10^{-1}$ $\pm 6.96 \times 10^{-2}$	$4.47 \times 10^{-1}$ $\pm 6.16 \times 10^{-2}$	$6.06 \pm 1.71$	$7.04 \pm 1.49$	21	25
	4	$2.98 \times 10^{-1}$ $\pm 4.69 \times 10^{-2}$	$2.60 \times 10^{-1}$ $\pm 4.13 \times 10^{-2}$	$4.02 \pm 0.99$	$3.84 \pm 1.05$	93	103
	5	$1.75 \times 10^{-1}$ $\pm 3.02 \times 10^{-2}$	$1.52 \times 10^{-1}$ $\pm 2.27 \times 10^{-2}$	$2.41 \pm 0.61$	$2.86 \pm 0.62$	284	259
	6	$1.06 \times 10^{-1}$ $\pm 1.58 \times 10^{-2}$	$9.69 \times 10^{-2}$ $\pm 1.24 \times 10^{-2}$	$1.98 \pm 0.41$	$1.84 \pm 0.38$	438	378
	7	$6.95 \times 10^{-2}$ $\pm 7.87 \times 10^{-3}$	$6.80 \times 10^{-2}$ $\pm 7.13 \times 10^{-3}$	$1.47 \pm 0.26$	$1.32 \pm 0.22$	397	243
	8	$5.27 \times 10^{-2}$ $\pm 2.19 \times 10^{-3}$	$4.96 \times 10^{-2}$ $\pm 2.50 \times 10^{-3}$	$1.07 \pm 0.17$	$0.98 \pm 0.13$	82	26
Significant fibrosis <i>6 weeks</i>	1	1.55	1.40	16.80	15.98	1	1
	2	$9.01 \times 10^{-1}$ $\pm 1.32 \times 10^{-1}$	$8.16 \times 10^{-1}$ $\pm 6.07 \times 10^{-2}$	$11.20 \pm 2.78$	$14.82 \pm 2.47$	8	6
	3	$4.63 \times 10^{-1}$ $\pm 7.47 \times 10^{-2}$	$4.72 \times 10^{-1}$ $\pm 9.39 \times 10^{-2}$	$7.29 \pm 1.84$	$7.02 \pm 1.78$	40	36
	4	$2.67 \times 10^{-1}$ $\pm 4.41 \times 10^{-2}$	$2.54 \times 10^{-1}$ $\pm 4.45 \times 10^{-2}$	$3.88 \pm 0.89$	$4.13 \pm 0.86$	159	147
	5	$1.57 \times 10^{-1}$ $\pm 2.54 \times 10^{-2}$	$1.44 \times 10^{-1}$ $\pm 2.32 \times 10^{-2}$	$2.92 \pm 0.61$	$2.97 \pm 0.62$	427	387
	6	$1.01 \times 10^{-1}$ $\pm 1.22 \times 10^{-2}$	$9.46 \times 10^{-2}$ $\pm 1.09 \times 10^{-2}$	$1.14 \pm 0.33$	$1.80 \pm 0.33$	596	419
	7	$7.24 \times 10^{-2}$ $\pm 6.74 \times 10^{-3}$	$6.96 \times 10^{-2}$ $\pm 4.19 \times 10^{-3}$	$1.57 \pm 0.22$	$1.30 \pm 0.22$	364	121
	8	$5.29 \times 10^{-2}$ $\pm 3.73 \times 10^{-3}$	$5.57 \times 10^{-2}$ $\pm 4.05 \times 10^{-3}$	$1.22 \pm 0.14$	$0.97 \pm 0.18$	56	36
Advanced fibrosis <i>12 weeks</i>	1	1.37	1.58	17.40	13.11	1	1
	2	$8.40 \times 10^{-1}$ $\pm 5.89 \times 10^{-2}$	$8.61 \times 10^{-1}$ $\pm 1.11 \times 10^{-1}$	$10.62 \pm 1.85$	$16.16 \pm 2.36$	7	6
	3	$5.03 \times 10^{-1}$ $\pm 7.40 \times 10^{-2}$	$4.56 \times 10^{-1}$ $\pm 6.61 \times 10^{-2}$	$6.42 \pm 1.64$	$7.02 \pm 1.66$	31	45
	4	$2.86 \times 10^{-1}$ $\pm 4.66 \times 10^{-2}$	$2.44 \times 10^{-1}$ $\pm 4.27 \times 10^{-2}$	$3.61 \pm 0.92$	$3.56 \pm 0.85$	130	166
	5	$1.68 \times 10^{-1}$ $\pm 2.74 \times 10^{-2}$	$1.40 \times 10^{-1}$ $\pm 2.10 \times 10^{-2}$	$2.81 \pm 0.63$	$2.28 \pm 0.50$	287	296
	6	$1.06 \times 10^{-1}$ $\pm 1.45 \times 10^{-2}$	$9.45 \times 10^{-2}$ $\pm 9.23 \times 10^{-3}$	$2.09 \pm 0.40$	$1.45 \pm 0.27$	380	170
	7	$7.10 \times 10^{-2}$ $\pm 8.37 \times 10^{-3}$	$6.64 \times 10^{-2}$ $\pm 7.79 \times 10^{-3}$	$1.52 \pm 0.27$	$1.18 \pm 0.21$	203	83

	8	$4.70 \times 10^{-2}$ $\pm 2.07 \times 10^{-3}$		$1.12 \pm 0.11$		10	
		Rat 7	Rat 8	Rat 7	Rat 8	Rat 7	Rat 8
Cirrhosis 18 weeks	1	1.71	1.01	18.21	17.64	1	1
	2	$9.35 \times 10^{-1}$ $\pm 6.85 \times 10^{-2}$	$6.73 \times 10^{-1}$ $\pm 6.01 \times 10^{-2}$	$13.50 \pm 2.92$	$11.80 \pm 1.75$	5	6
	3	$5.53 \times 10^{-1}$ $\pm 8.51 \times 10^{-2}$	$4.05 \times 10^{-1}$ $\pm 5.90 \times 10^{-2}$	$9.47 \pm 1.90$	$5.93 \pm 1.21$	19	23
	4	$3.25 \times 10^{-1}$ $\pm 5.36 \times 10^{-2}$	$2.50 \times 10^{-1}$ $\pm 4.07 \times 10^{-2}$	$4.11 \pm 1.13$	$4.57 \pm 1.06$	93	67
	5	$1.96 \times 10^{-1}$ $\pm 3.14 \times 10^{-2}$	$1.55 \times 10^{-1}$ $\pm 2.16 \times 10^{-2}$	$2.70 \pm 0.69$	$3.43 \pm 0.75$	215	121
	6	$1.21 \times 10^{-1}$ $\pm 1.67 \times 10^{-2}$	$1.02 \times 10^{-1}$ $\pm 1.06 \times 10^{-2}$	$2.35 \pm 0.52$	$2.00 \pm 0.49$	360	127
	7	$8.62 \times 10^{-2}$ $\pm 7.22 \times 10^{-3}$	$7.64 \times 10^{-2}$ $\pm 6.38 \times 10^{-3}$	$1.78 \pm 0.34$	$1.51 \pm 0.40$	163	53
	8	$6.61 \times 10^{-2}$ $\pm 5.53 \times 10^{-3}$	$5.78 \times 10^{-2}$ $\pm 3.87 \times 10^{-3}$	$1.20 \pm 0.23$	$1.02 \pm 0.13$	75	20

484

485

486 **Table 3:** Macroscopic hepatic arteries were classified according to their diameter-defined  
 487 branching topology at different time points during cirrhogenesis. The mean radius, mean length  
 488 and number of vessels were measured based on the assignment of generation numbers.

HA	Generation	Mean radius (mm)		Mean length (mm)		#Vessels	
		Rat 1	Rat 2	Rat 1	Rat 2	Rat 1	Rat 2
Healthy liver <i>0 weeks</i>	1	$1.74 \times 10^{-1}$	$1.71 \times 10^{-1}$	4.97	9.04	1	1
	2	$1.11 \times 10^{-1}$ $\pm 1.28 \times 10^{-2}$	$9.60 \times 10^{-2}$ $\pm 8.61 \times 10^{-3}$	$11.69 \pm 1.79$	$7.16 \pm 2.59$	4	3
	3	$7.74 \times 10^{-2}$ $\pm 8.56 \times 10^{-3}$	$7.34 \times 10^{-2}$ $\pm 6.46 \times 10^{-3}$	$7.75 \pm 1.78$	$10.45 \pm 2.24$	9	6
	4	$5.91 \times 10^{-2}$ $\pm 4.30 \times 10^{-3}$	$5.73 \times 10^{-2}$ $\pm 3.44 \times 10^{-3}$	$6.89 \pm 1.20$	$6.58 \pm 1.48$	13	7
	5	$4.54 \times 10^{-2}$ $\pm 3.28 \times 10^{-3}$	$4.81 \times 10^{-2}$ $\pm 1.88 \times 10^{-3}$	$2.59 \pm 0.61$	$8.08 \pm 2.27$	20	17
Significant fibrosis <i>6 weeks</i>	1	$1.82 \times 10^{-1}$	$1.82 \times 10^{-1}$	6.23	15.49	1	1
	2	$1.10 \times 10^{-1}$ $\pm 1.19 \times 10^{-2}$	$1.35 \times 10^{-1}$ $\pm 8.12 \times 10^{-3}$	$11.68 \pm 2.73$	$3.83 \pm 0.76$	5	3
	3	$6.92 \times 10^{-2}$ $\pm 9.46 \times 10^{-3}$	$7.98 \times 10^{-2}$ $\pm 1.24 \times 10^{-2}$	$12.10 \pm 2.59$	$11.45 \pm 2.47$	9	13
	4	$5.13 \times 10^{-2}$ $\pm 2.88 \times 10^{-3}$	$5.26 \times 10^{-2}$ $\pm 4.69 \times 10^{-3}$	$5.58 \pm 1.11$	$5.05 \pm 1.17$	12	21
	5	$4.46 \times 10^{-2}$ $\pm 7.64 \times 10^{-4}$	$4.20 \times 10^{-2}$ $\pm 1.55 \times 10^{-3}$	$6.28 \pm 1.94$	$2.94 \pm 0.79$	12	7
Advanced fibrosis <i>12 weeks</i>	1	$2.06 \times 10^{-1}$	$2.35 \times 10^{-1}$	2.90	3.99	1	1
	2	$1.37 \times 10^{-1}$ $\pm 1.55 \times 10^{-3}$	$1.78 \times 10^{-1}$ $\pm 1.77 \times 10^{-2}$	$4.85 \pm 1.41$	$9.11 \pm 0.79$	2	2
	3	$8.20 \times 10^{-2}$ $\pm 7.40 \times 10^{-3}$	$1.16 \times 10^{-1}$ $\pm 1.08 \times 10^{-2}$	$11.38 \pm 2.31$	$13.94 \pm 2.53$	7	10
	4	$6.04 \times 10^{-2}$ $\pm 3.76 \times 10^{-3}$	$9.04 \times 10^{-2}$ $\pm 6.92 \times 10^{-3}$	$9.93 \pm 2.17$	$7.68 \pm 0.48$	11	16
	5	$4.7 \times 10^{-2}$ $\pm 2.72 \times 10^{-3}$	$6.53 \times 10^{-2}$ $\pm 5.58 \times 10^{-3}$	$4.08 \pm 0.88$	$3.30 \pm 0.96$	7	14
Cirrhosis <i>18 weeks</i>	1	$3.01 \times 10^{-1}$	$2.69 \times 10^{-1}$	20.40	14.04	1	1
	2	$1.85 \times 10^{-1}$ $\pm 1.25 \times 10^{-2}$	$1.87 \times 10^{-1}$ $\pm 1.51 \times 10^{-2}$	$6.47 \pm 1.30$	$13.30 \pm 2.53$	5	4
	3	$1.37 \times 10^{-1}$ $\pm 1.56 \times 10^{-2}$	$1.30 \times 10^{-1}$ $\pm 1.22 \times 10^{-2}$	$8.63 \pm 2.21$	$7.25 \pm 1.79$	11	16
	4	$9.87 \times 10^{-2}$ $\pm 7.25 \times 10^{-3}$	$9.79 \times 10^{-2}$ $\pm 1.21 \times 10^{-2}$	$6.15 \pm 1.52$	$5.23 \pm 1.29$	18	32
	5	$7.27 \times 10^{-2}$ $\pm 6.57 \times 10^{-3}$	$7.23 \times 10^{-2}$ $\pm 6.16 \times 10^{-3}$	$3.14 \pm 0.96$	$2.92 \pm 1.07$	31	24
	6	$5.38 \times 10^{-2}$ $\pm 5.57 \times 10^{-3}$	$5.52 \times 10^{-2}$ $\pm 5.82 \times 10^{-3}$	$1.73 \pm 0.60$	$1.83 \pm 0.44$	12	25

489